# Synthesis of Supported Catalysts by Dry Impregnation in Fluidized Bed

Laurie Barthe, Serge Desportes, Mehrdji Hemati, Karine Philippot, Bruno Chaudret

# SYNTHESIS OF SUPPORTED CATALYSTS BY DRY IMPREGNATION IN FLUIDIZED BED

**L. Barthe[1], S. Desportes[1], M. Hemati[1,*], K. Philippot[2] and B. Chaudret[2]**

[1]Laboratoire de Génie Chimique, Toulouse, France.
[2]Laboratoire de Chimie de Coordination, Toulouse, France.

**Abstract:** The synthesis of catalytic or not composite materials by dry impregnation in fluidized bed is described. This process can be carried out under mild conditions from solutions of organometallic precursors or colloidal solutions of preformed nanoparticles giving rise to reproducible metallic nanoparticles containing composite materials with a high reproducibility. The adequate choice of the reaction conditions makes possible to deposit uniformly the metal precursor within the porous matrix or on the support surface. When the ratio between the drying time and the capillary penetration time ($t_{sec}/t_{cap}$) is higher than 10, the impregnation under soft drying conditions leads to a homogeneous deposit inside the pores of the particles of support. The efficiency of the metal deposition is close to 100%, and the size of the formed metal nanoparticles is controlled by the pores diameter.

Finally, some of the presented composite materials have been tested as catalysts: iron-based materials were used in carbon-nanotubes synthesis, while Pd and Rh composite materials have been investigated in hydrogenation reactions.

**Keywords:** metallic nanoparticles; porous supports; supported catalysts; fluidized bed; dry impregnation; composite materials.

## INTRODUCTION

The preparation of composite materials by dry impregnation of porous particles can be carried out in a fluidized bed. This technique permits to make, in only one apparatus, composite materials which, by the usual way, would successively undergo the stages of impregnation, filtration, drying and calcination/activation.

The principle of this technique consists in spraying a solution containing a metallic precursor into a hot fluidized bed of porous fine particles. After the impregnation step, metallic precursor decomposition and metal activation can be performed in the same reactor. In the case of organometallic complexes, the decomposition/activation is achieved at low temperature ($T < 80^{\circ}C$) under a reactive atmosphere ($H_2/N_2$ mixture), while for inorganic precursors, calcination is realized at high temperature ($T > 450^{\circ}C$) without changing the atmosphere composition.

Previous studies performed in our research team have shown the feasibility of manufacturing catalysts by direct impregnation of porous support through pulverization of metallic precursor solutions in a hot fluidized bed (Hemati *et al.*, 2001, 2003; Desportes *et al*., 2005). From these results one could conclude that, according to the operation conditions, the pulverization of a metallic salt aqueous solution on porous particles can lead to two different cases:

- in conditions of soft drying, homogenous impregnation;
- in conditions favouring fast evaporation of solvent, deposit on the external surface of the support.

These studies have shown that solute distribution inside porous solid particles depends on two characteristic times:

- $t_{cap}$, the wetting time or capillary penetration time. It corresponds to the time which is necessary for the liquid to go from the external surface towards the particle centre. This value is calculated from the following equation (1):

$$t_{cap} = \frac{2\mu l^2}{\gamma_{LV} \cos\theta r_{pore}} \quad (1)$$

  where $\mu$ is the liquid viscosity, $l$ the pore length equivalent to the radius particle multiplied by the tortuosity factor, $\gamma_{LV}$ the interfacial tension, $\theta$ the contact angle and $r_{pore}$ pore radius.
- $t_{sec}$, the drying time. It is defined as the time necessary for a particle saturated by pure solvent to be transformed into a dry particle under fluidized bed conditions (temperature and humidity). The calculation of this

*Correspondence to:
Professor M. Hemati, Laboratoire de Génie Chimique-UMR CNRS 5503-INP-ENIACET, 5 rue Paulin Talabot, BP 1301, 31106 Toulouse Cedex 01, France.
E-mail: mehrdji.hemati@ensiacet.fr

characteristic time is based on the mass and energy balances on a single wetted particle considering that the mass transfer is controlled by external resistance (gas phase). The model's equations are presented in Appendix A.

The solute distribution can be considered as uniform when the ratio between these two characteristic times becomes higher than 10 (Desportes, 2005)

To determine the best operative conditions and to check the deposit location, deposition of manganese nitrate was realized on coarse alumina particles (sized around 2.4 mm) (Desportes, 2005). This size of particles was chosen for an easier observation of the metal deposit. Two experiments were performed: sample F, corresponding to fast drying (low liquid flow rate, low gas relative humidity in the reactor) and sample S, corresponding to soft drying (high liquid flow rate and high gas relative humidity in the reactor). Observation of these samples in Figure 1 by video microscopy showed that in the case of sample F, the deposit takes place only at the surface of solid particles, while for sample S, the solute enters in particles according to a front which moves from external to central area, during the impregnation. At the end of the operation (S3), the so-obtained catalysts are uniform.

This work gathers experiments carried out to prepare composite materials, using various types of precursors: metallic salts or metal organic precursors solutions and colloidal suspensions containing preformed metal nanoparticles. It is divided in two parts: the first one deals with the synthesis and the characterization of composite materials and the second with catalysis applications.

## METHODS AND MATERIALS

### Experimental Set-Up

Experiments were carried out in two different batch fluidized beds working on the same principle. One, installed in a glove box, allows syntheses under controlled atmosphere (inert or reductive) depending on the nature of metal precursor, with reduced quantity of precursor, since it operates at laboratory scale (production of catalyst: 30–100 g).

The second one is ATEX norms respectful and can treat a more important quantity of powder. It is presented in Figure 2. The reactor is a stainless steel cylindrical column with a 0.1 m inner diameter and 0.5 m in height. The gas distributor is a stainless steel perforated plate with a porosity of 0.5% (12 holes of 1 mm, organized according to a triangular mesh of 5 mm step). Before entering the bed, the fluidizing gas flow rate is measured by a rotameter and preheated by an electrical heater. At the outlet of the column, the elutriated particles are separated from the gas phase by a cyclone. The solvent vapours are collected by a condenser. The metallic precursor solution is drawn up by a volumetric pump from a reservoir to a spray nozzle. The atomizer is a downward facing nozzle and is located in the bed (Saleh *et al*., 1999). The bed temperature is controlled by means of a PID regulator. Temperature and pressure drop are monitored all operation long.

The general experimental protocol is as follows:

- The column is initially charged with a calculated mass of porous particles.
- The powder is fluidized by a fixed hot gas flow rate.
- The pure solvent is sprayed within the bed, at the same flow rate as the metallic precursor solution.
- As soon as the thermal steady state regime is reached, the solvent is replaced by the solution containing metallic precursor. Solid samples can be taken at different times to follow the impregnation kinetic.
- At the end of the impregnation step, the decomposition/activation of the precursor is carried out by stopping spraying and by increasing the bed temperature in the column. The fluidization gas, a H2/N2 mixture (10/90 v/v) which allows to generate metal nanoparticles from the metallic precursor. In the case of metal organic precursors this decomposition/activation step is carried out at low temperature (80°C).

Fine porous silica particles (silica gel Merck 60) are used as catalysts support. Their physical properties are listed in Table 1.

### Characterization Methods

All the samples were characterized using different techniques in order to determine their characteristics:

- Particles morphology and topology, and the size of metal nanoparticles were studied respectively by scanning electron microscope (SEM) and transmission electron microscope (TEM) equipped with chemical element detector (XRD). This information permit to understand the surface morphology and the chemical element distribution on the solid cross-sectional.
- Particles mean diameter and size distribution were estimated by laser granulometry.

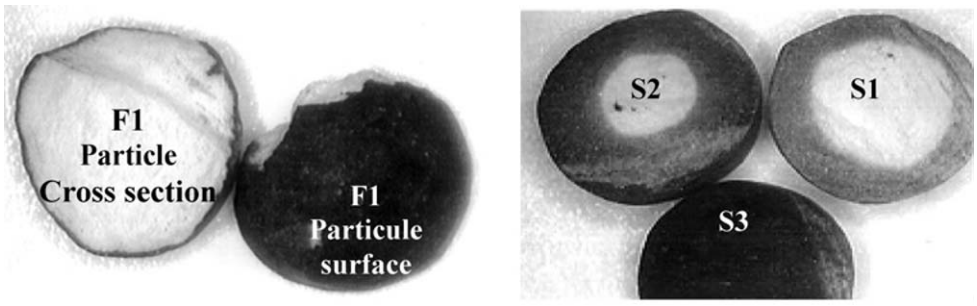


*Figure 1.* Video microscope micrographs of cross section surface of samples F and S1–S3.

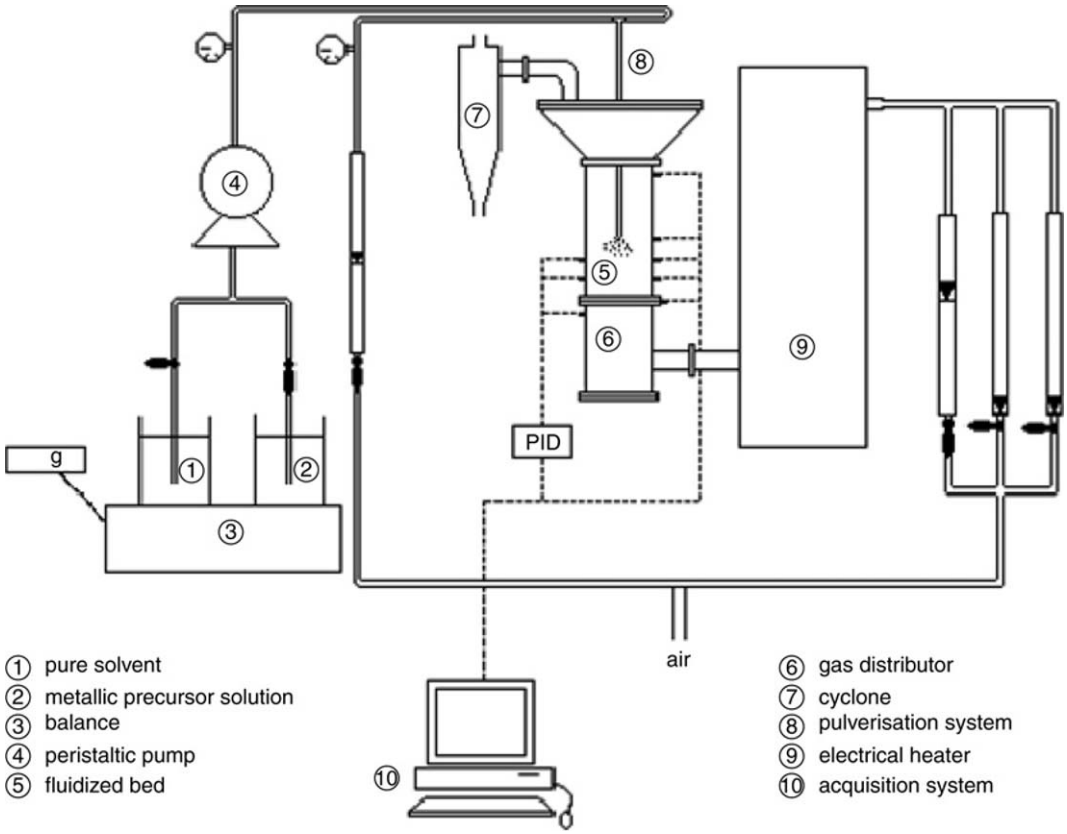


*Figure 2.* Schematization of the fluidized bed respecting ATEX norms.

*Table 1.* Physical properties of silica gel

| Properties | Silica gel |
|---|---|
| Mean diameter (μm) | 90 |
| $S_{BET}$ ($m^2\ g^{-1}$) | 530 |
| Porous volume ($ml\ g^{-1}$) | 0.66 |
| Average pore diameter (Å) | 55 |
| Real density ($kg\ m^{-3}$) | 2260 |
| Apparent density ($kg\ m^{-3}$) | 910 |
| Internal porosity (%) | 60 |
| $U_{mf}$ at 25°C (minimal fluidization velocity) ($m\ s^{-1}$) | 0.0028 |
| $U_t$ at 25°C (terminal velocity) ($m\ s^{-1}$) | 0.19 |

- Samples specific area and pore size distribution were determined by the BET standard method ($N_2$ adsorption–desorption).
- Apparent and skeletal densities were obtained with helium pycnometry and pore volume with mercury porosimetry.
- Crystalline phases were evaluated by X-ray diffraction.
- Metal loading of composite materials was determined by elemental analysis.

From metal contents measurements by elemental analysis, the experimental deposit rate $\tau_{real}$ can be estimated.

A theoretical deposit rate $\tau_{theo}$ is also defined and corresponds to the relationship (2) between the quantity of precursor sprayed during a time $t$ and the mass of support present in the fluidized bed.

$$\tau_{theo} = 100\frac{\dot{m}_{so} C_l t}{m_s} \tag{2}$$

where, $\dot{m}_{so}$ is the solution mass flow rate, $c_l$ the precursor concentration, $t$ operation time, $m_s$ the initial weight of solid particles in the bed.

The deposit efficiency is calculated, relationship (3), considering the ratio between experimental deposit rate ($\tau_{real}$) and theoretical deposit rate ($\tau_{theo}$).

$$\text{Efficiency} = \frac{\tau_{real}}{\tau_{theo}} \tag{3}$$

## Experiments

The reaction conditions are listed in Table 2. The first fourth experiments were carried out with inorganic precursors. Organometallic complexes have been used in experiments 5 and 6 while for experiment 7 a colloidal suspension has been sprayed. The pure solvent used is water except for experiments 5 and 6 for which tetrahydrofuran (THF) has been used since these precursors are water sensitive.

Operation conditions have been chosen to obtain the ratio $t_{sec}/t_{cap}$ widely higher than 10 in order to favour metal deposition within the porous matrix, except for experiment 6 where the ratio $t_{sec}/t_{cap}$ is set to 7.

*Table 2.* Experimental conditions

| Experiment number | 1 | 2 | 3 | 4 | 5 | 6 | 7 |
|---|---|---|---|---|---|---|---|
| Precursors name | Copper nitrate | Nickel nitrate | Manganese nitrate | Iron nitrate | Iron amide | Palladium allyl chloride | Rhodium suspension |
| Precursors formula | $Cu(NO_3)_2$, $4H_2O$ | $Ni(NO_3)_2$, $6H_2O$ | $Mn(NO_3)_2$, $4H_2O$ | $Fe(NO_3)_2$, $9H_2O$ | $Fe[N(SiMe_3)_2]_2$ | $[PdCl(C_3H_5)]_2$ | — |
| Precursor concentration (%) | 33 | 15 | 20 | 30 | 33 | 1.1 | — |
| Solvent nature | Water | Water | Water | Water | THF | THF | Water |
| Gas flow rate ($m^3\ h^{-1}$) | 7.4 | 4.3 | 4.8 | 1.1 | 0.8 | 0.8 | 0.8 |
| Temperature gas entrance (°C) | 230 | 145 | 166 | 160 | 180 | 180 | 170 |
| Fluidized bed temperature (°C) | 70 | 70 | 58 | 36 | 23 | 25 | 40 |
| Final metal loading (%) | 4.6 | 3.9 | 5.2 | 4.1 | 3.3 | 3.8 | 0.08 |
| Final deposit rate (%) | 55 | 10 | 42 | 23 | 5 | 9 | 1 |
| $t_{sec}/t_{cap}$ | 100 | 73 | 210 | 390 | 35 | 7 | 580 |

## RESULTS AND DISCUSSION

### Composite Materials Synthesis

The characterization results obtained from produced composite materials led to general conclusions hereafter presented.

#### *Efficiency*

The theoretical and experimental deposit rates evolution during time is presented in Figure 3 for four different cases.

These deposit rates vary in a linear way during spraying and are very close to each other, showing that the efficiency of the deposit is close to 100%, without any loss of precursor. Thus, at fixed precursor concentration, spraying time controls the deposit quantity.

#### *Deposit localization and uniformity*

Granulometry analysis shows that the mean diameter (d50) of several samples oscillates around the mean initial diameter support value. In the same way, particles size distribution remains unchanged as shown in Figure 4. Thus, there is neither an increase of particles size nor an agglomeration phenomenon. This proves that the deposit takes place inside the particles.

To confirm this hypothesis, pore size distribution, specific area and internal porosity have been determined by BET (Figures 5 and 6). These analyses have been performed on the calcinated samples.

The conservation of the pore size distribution pattern between the initial support and samples resulting from impregnation at different metal loading [Figure 5(a) and (b)] is observed.

Moreover, specific area and internal porosity decrease regularly according to the spraying time, i.e., the increasing of metal loading, as shown in Figure 6.

Results enable us to consider that the deposit is homogenous and inside the inorganic support. The solute distribution can be considered as almost uniform in the solid.

#### *Deposit morphology*

The deposit morphology of palladium- and iron-based composite materials has been studied after an activation step leading to the formation of metal nanoparticles. In the case of organometallic precursors this activation step is operated under a nitrogen/hydrogen mixture at 80°C during 90 min, while for inorganic precursors the samples are heated up to 450°C in air.

Two examples are presented. The first one, palladium-based composite materials using the $[PdCl(allyl)]_2$ organometallic complex as metal source, has been characterized by TEM and XRD, to respectively determine metal nanoparticles size and their dispersion inside the porous support, and their crystalline structures. From the diffraction diagram of Figure 7, we can deduce that nanoparticles of non-oxidized and crystalline Pd metal with an estimated mean size of 6–7 nm have been obtained within the porous matrix.

TEM micrographs, registered after ultramicrotomy preparation of $SiO_2$/Pd sample, corresponding to different areas of the particles observed (centre, periphery and surface) are presented in Figures 8 and 9. These figures show that:

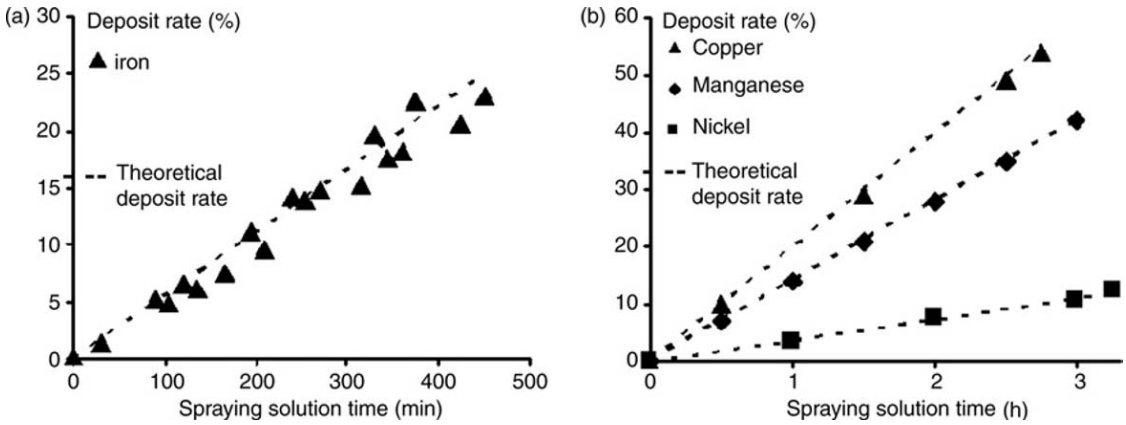


*Figure 3.* Deposit rate evolution versus spraying solution time, in case of iron based composite material (a) and copper-, manganese- and nickel-based composite materials (b).

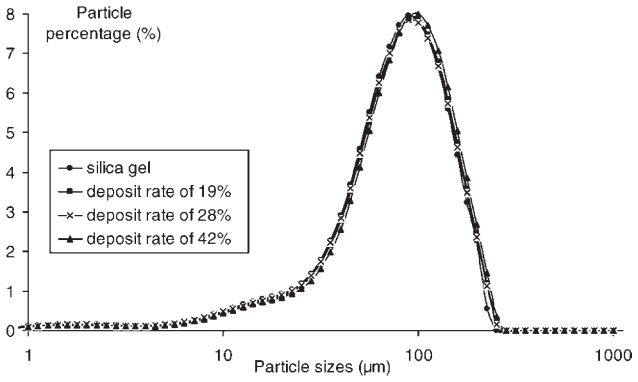


*Figure 4.* Particles size distribution for different metal loading.

- In central area of silica particles, the deposit is uniform with isolated Pd nanoparticles [Figure 8(a)]. The size distribution, obtained from diameter measurement of 140 nanoparticles [Figure 8(b)], indicates that the Pd nanoparticles are monodisperse and display a mean size of 7 nm.
- At the periphery of the support particles, the Pd nanoparticles are assembled into packets and form a sort of fractal structures (Figure 9).
- At the surface, a similar structure is found.

Secondly, TEM analyses carried out on iron based composite materials after ultramicrotomy preparation revealed well-dispersed iron nanoparticles in silica (Figure 10). The measurement of a great number of nanoparticles permits to estimate that they have a homogeneous size distribution around 5 nm.

### *Colloidal suspension spraying*

To demonstrate the feasibility of dry impregnation of porous particles by a colloidal suspension, a set of experiments have been performed using a colloidal suspension containing rhodium nanoparticles (mean size 5 nm). The operational conditions are listed in Table 2. The granulometry analysis shows that there is no modification of the particles average size, neither of the size distribution. Elemental analysis confirms that the deposit efficiency is about 100%. Then, particles surface and cross section are observed with different microscopy techniques (TEM, SEM), coupled with the XRD

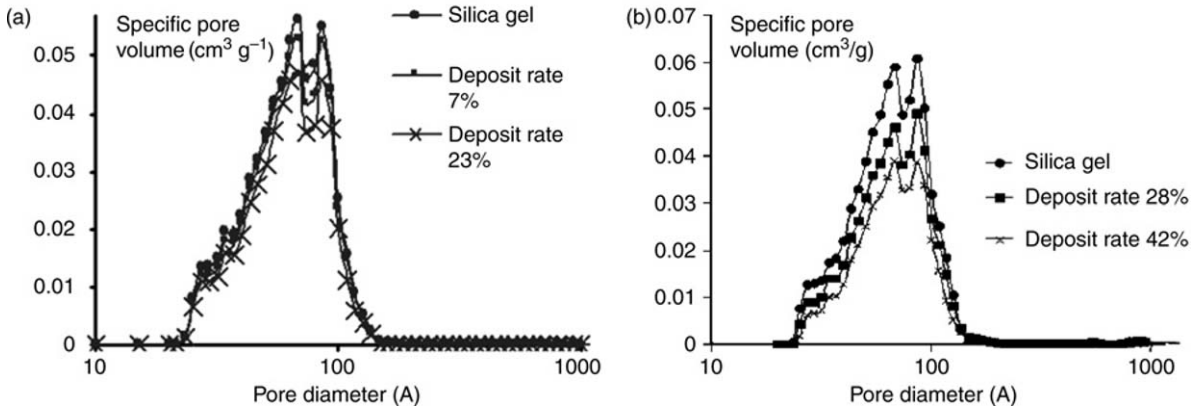


*Figure 5.* Pore size distribution for different metal loading in case of (a) iron composite materials on silica gel (b) manganese composite materials on silica gel.

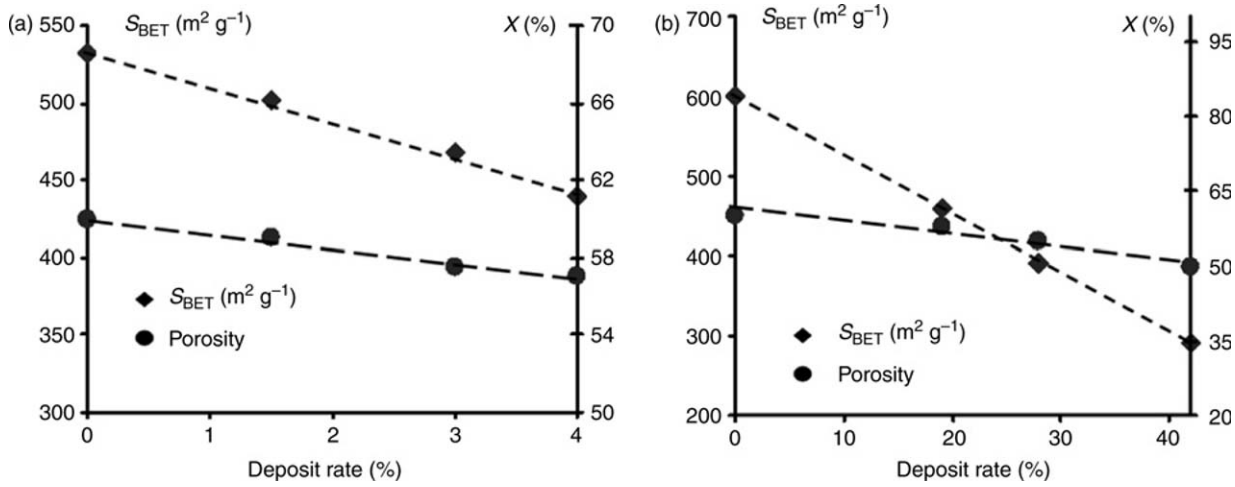


*Figure 6.* Specific surface and internal porosity versus deposit rate for sample of (a) iron composite material supported on silica gel (b) manganese composite material supported on silica gel.

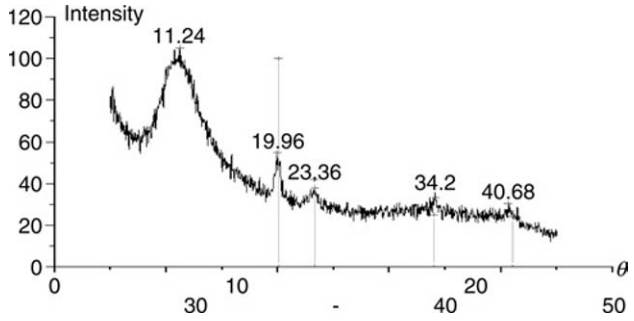


*Figure 7.* X-ray diffraction diagram obtained for Pd samples (face centred cubic, fcc).

analysis (Figure 11). The results show that the rhodium nanoparticles deposition takes place within the silica particles with a good dispersion. Their mean size is about 5 nm. This value is close to that measured in the initial colloidal suspension. The metal nanoparticles deposition can then be considered as homogeneous.

## Applications

Taking into account that such metal composite materials could find application in the field of catalysis, some of them were investigated in catalytic reactions. First of all, iron composite materials have been tested as catalysts for the synthesis of carbon nanotubes. Then, palladium, rhodium and nickel samples have been used in hydrogenation reactions. Preliminary results are shown hereafter.

### *Carbon nanotubes synthesis*

For the synthesis of carbon nanotubes, two iron supported catalysts samples were tested: one obtained by spraying iron nitrate aqueous solution (cat 1) and the second resulting from an iron amide metallic precursor containing solution (cat 2).

The catalytic tests were made at the 'Laboratoire de Catalyse Chimie Fine et Polymère' of Toulouse (LCCFP) by

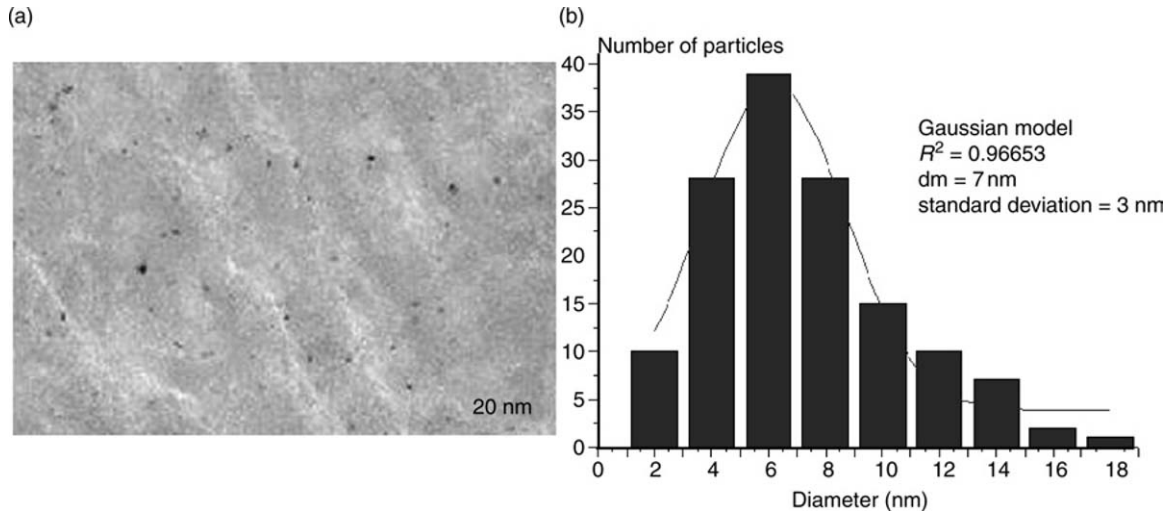


*Figure 8.* Pd material composite observed in central area of silica particles (a) TEM micrograph (b) nanoparticles size distribution.

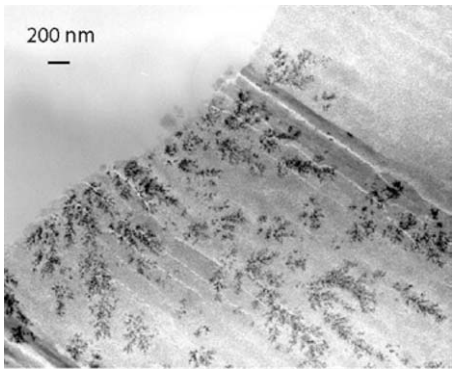


*Figure 9.* TEM micrograph of Pd material composite observed at the surface of silica particles.

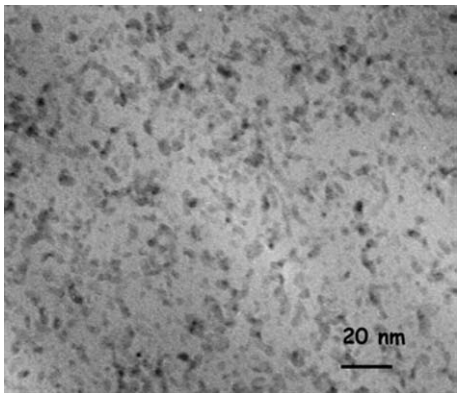


*Figure 10.* TEM micrograph of iron material composite supported on silica after ultramicrotomy.

Lamouroux (2005). One-hundred milligrams of each catalyst were placed in a small alumina capsule in the centre of a plan reactor. An increase of the reactor temperature during 1 h was performed. When a temperature of 900°C was reached, a $N_2/H_2/CH_4$ (50/150/100 sccm) gas flow mixture was introduced during 30 min. At the end of the reaction, a flow rate of $N_2$ of 200 sccm was introduced in the reactor until the system comes back to ambient temperature.

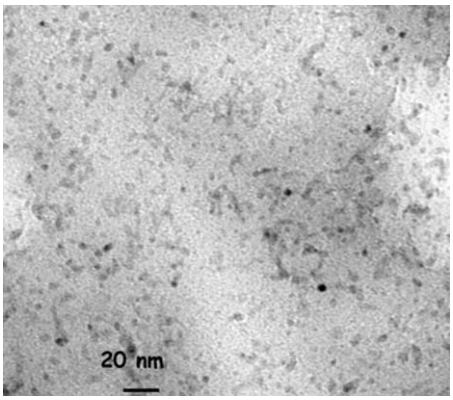


*Figure 11.* TEM micrograph of Rhodium composite material obtained by spraying colloidal Rh suspension on silica gel after ultramicrotomy preparation.

Catalysts prepared by dry impregnation in fluidized bed lead to a good selectivity and a good catalytic activity for the carbon nanotubes synthesis [Figure 12 (a) and (b)].

On this figure, one can see that catalyst cat 1 allows to obtain a majority of single wall carbon nanotubes (12a) while cat 2 a majority of double wall carbon nanotubes (12b).

### *Selective hydrogenation catalysis*

The rhodium composite material, resulting from impregnation of colloidal rhodium suspension has been evaluated as hydrogenation catalyst in the 'Synthèse Organique et Systèmes Organisés' in Rennes (SOSO). The catalyst has been tested in orthoxylene hydrogenation. Reaction pathway (4) is hereafter presented:

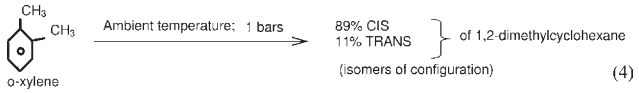


(4)

At ambient temperature and atmospheric $H_2$ pressure, this catalyst presents a conversion of 98% after 2 h and a very good selectivity (92%) for Cis 1,2-dimethylcyclohexane. These results are closed to the ones obtained with colloidal suspension of rhodium (Roucoux *et al*., 2002).

Moreover, palladium composite materials were tested in hydrogenation of ethyl pyruvate. Reaction pathway is as follows (5):

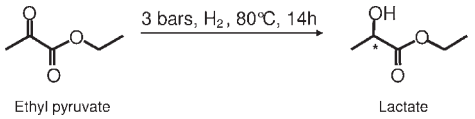


(5)

At 80°C and under 3 bars of dihydrogen, this catalyst presents a good activity with 95% of conversion after 14 h.

Thus, activities of nickel-based composite materials (cat a; Table 3 test numbers 1–5) were determined in hydrogenation of hexene into hexane and compared with the activity of another nickel-based catalyst obtained by classical impregnation (CI; Table 3 test number 6). Results are described in the first part of Table 3 and show that the reaction, in these reaction conditions, is fast.

For this reaction, the composite materials elaborated in a fluidized bed have an activity comparable to those of supported catalyst prepared by a classical way.

The catalytic activity of nickel-based composite materials (cat a) in hexene hydrogenation was compared to the one of a palladium-based composite material obtained from a metal organic precursor (both produced by dry impregnation) (second part of Table 3).

It appears that palladium-based composite materials display a conversion similar to that of cat a, but at smaller metal loading (0.1% in place of 0.5%). This shows the interest of using palladium-based composite materials, produced in mild conditions from an organometallic precursor.

## CONCLUSION

In this paper, the synthesis and the characterization of metal-based composite materials obtained by dry

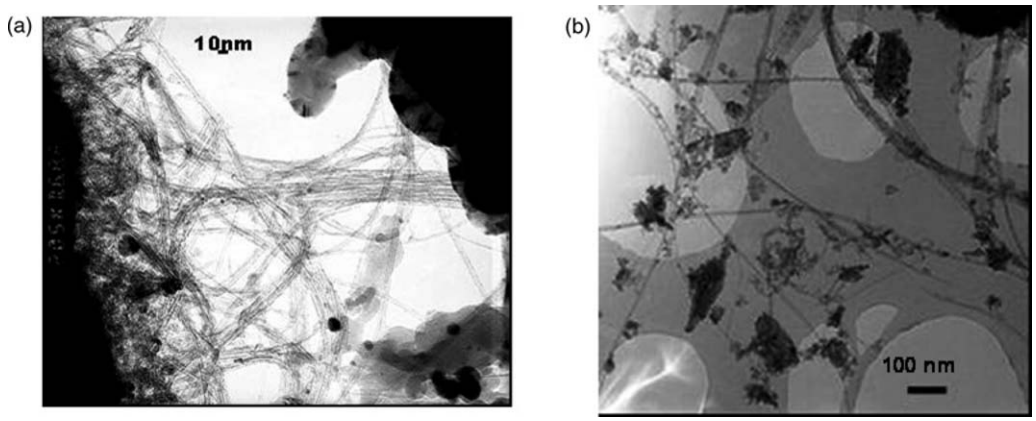


*Figure 12.* TEM micrographs of carbon nanotubes (a) single wall carbon nanotubes (SWNT) (cat 1) (b) double wall carbon nanotubes (DWNT) (cat 2).

*Table 3.* Results of hexene hydrogenation

| Test number | Metal loading (%) | Catalyst mass (mg) | Reaction time (h) | Conversion (%) |
|---|---|---|---|---|
| 1 | 8 | 5 | 5 | 99.9 |
| 2 | 8 | 5 | 4 | 99 |
| 3 | 8 | 5 | 3 | 99 |
| 4 | 8 | 5 | 2 | 99 |
| 5 | 5 | 10 | 4 | 90 |
| 6 (Cl) | 4 | 10 | 4 | 94 |
| 7 | 0.5/Ni | 100 | 4 | 99 |
| 8 | 0.5/Pd | 170 | 4 | 100 |
| 9 | 0.1/Pd | 850 | 4 | 95 |

impregnation in a fluidized bed from different metal precursors are described. In all cases, the deposition efficiency is closed to 100%. The results evidence that the location of the metal deposition can be controlled depending on the reaction conditions. Moreover, the metal deposit within the porous network or on the surface is almost uniform. In addition, it has been shown that a colloidal metal suspension can be used for the impregnation of a porous inorganic support. Finally, some of the so-obtained composite materials were tested as catalysts and the preliminary results revealed interesting catalytic properties. The fact that the composite materials are prepared in only one apparatus and that the set-up of reaction conditions allows to control the metal deposit at the porous particle scale appear as the main advantages of this technique.

## NOMENCLATURE

| | |
|---|---|
| $c_l$ | precursor concentration in the solution, kg kg$^{-1}$ of solvent |
| $Cp$ | specific heat, J kg$^{-1}$ K$^{-1}$ |
| $He$ | enthalpy, J kg$^{-1}$ |
| $h$ | convective heat transfer coefficient, W m$^{-2}$ K$^{-1}$ |
| $k_y$ | mass transfer coefficient, kg s$^{-1}$ m$^{-2}$ |
| $l$ | pore length, $\mu$m |
| $M$ | molecular weight, kg mol$^{-1}$ |
| $\dot{m}$ | mass flow rate, kg s$^{-1}$ |
| $m_p^{sec}$ | mass of a dry particle, kg |
| $m_s$ | initial weight of solid particles, kg |
| $P_{ref}$ | reference pressure, Pa |
| $P_{atm}$ | atmospheric pressure, Pa |
| $P^{0V}$ | saturation vapour pressure, Pa |
| $P_t$ | total pressure in the reactor, Pa |
| RH | relative humidity, % |
| $r_{pore}$ | pore radius, Å |
| $S_{BET}$ | specific area, m$^2$ g$^{-1}$ |
| $S_p$ | external surface of a particle, m$^2$ |
| $T$ | temperature, K |
| $T_p$ | particle temperature, K |
| $T_{ref}$ | reference temperature, K |
| $t$ | operation time, s |
| $t_{cap}$ | wetting time or capillary penetration time, s |
| $t_{sec}$ | drying time, s |
| $U_{mf}$ | minimal fluidization velocity (at 25°C), m s$^{-1}$ |
| $U_t$ | terminal velocity (at 25°C), m s$^{-1}$ |
| $V_p$ | volume of a particle, m$^3$ |
| $X$ | solid solvent content, kg solvent/kg$^{-1}$ dry particle |
| $w_l$ | solution mass flow rate, kg min$^{-1}$ |
| $\bar{Y}$ | average solvent content, kg solvent kg$^{-1}$ dry gas |
| $Y$ | solvent content, kg solvent kg$^{-1}$ dry gas |
| $Y^\circ$ | maximal solvent content in the reactor, kg solvent kg$^{-1}$ dry gas |

*Greek symbols*

| | |
|---|---|
| $\gamma_{LV}$ | liquid–gas interfacial tension, N m$^{-1}$ |
| $\theta$ | contact angle, radian |
| $\mu$ | liquid viscosity, Pa s |
| $\rho$ | density, kg m$^{-3}$ |
| $x$ | internal porosity, % |
| $\Delta H_v$ | solvent evaporation enthalpy, J kg$^{-1}$ |
| $\Delta H_v^0$ | solvent evaporation enthalpy at 0°C, J kg$^{-1}$ |
| $\tau_{real}$ | experimental deposit rate, % |
| $\tau_{theo}$ | theoretical deposit rate, % |
| $\tau_{sat}$ | saturation rate, % |
| $\Phi_{th}$ | heat flow, W |

*Subscripts*

| | |
|---|---|
| ato | atomization gas |
| bed | bed of particles |
| g | dry gas |
| l | interface |
| pr | precursor |
| s | solid |
| sl | solvent |
| so | solution |

*Superscripts*

| | |
|---|---|
| *e* | entry |
| *g* | gas state |
| *l* | liquid state |
| *s* | out |
| *sec* | dry |
| *vap* | vapour state |

*Adimensional numbers*

| | |
|---|---|
| *Le* | Lewis |
| *Pr* | Prandtl |
| *Sc* | Schmidt |

## REFERENCES


Cobbinah, S.S., 1984, Analyse des phéomèes couplé de transfert de chaleur et de matiée à l';extéieur et l'intéieur de grosses particules humides séchées par immersion dans un lit fluidisé de fines, PhD thesis, INP Toulouse, France.

Desportes, S., 2005, Imprénation en voie sèche en lit fluidisé application à la synthèse de catalyseurs supportés, PhD thesis, INP Toulouse, France.

Desportes, S., Steinmetz, D., Hemati, M., Philippot, K. and Chaudret, B., 2005, Production of supported asymmetric catalysys in a fluidized bed, *Powder Technol*, 157: 12–19.

Hemati, M., Cherif, R., Saleh, K. and Pont, V., 2003, Fluidized bed coating and granulation: influence of process-related variables and physicochemical properties on the growth kinetics, *Powder Technol*, 130: 18–34.

Hemati, M., Steinmetz, D., Chaudret, B. and Philippot, K., 2001, Fabrication de catalyseur d'un nouveau type par imprénation en lit fluidisé Brevet EPI-PCT/FR 02/01795.

Lamouroux, E., 2005, Synthèe de nanotubes de carbone mono-parois, préaration de catalyseurs à base de fer supportés sur alumine par dépôt en phase vapeur à partir de complexes organoméalliques, PhD thesis, UPS Toulouse, France.

Roucoux, A., Jügen, S., Patin, H. *et al*., 2002, Stabilized rhodium (o) nanoparticles: a reusable hydrogenation catalyst for arene derivatives in a biphasic water-liquid system, *Chem A Eur J*, 2000 6(4): 618–624.

Saleh, K., Cherif, R. and Hemati, M., 1999, Coating of solid particles in a fluidized bed. Influence of operating conditions on growth kinetics, *Advanced Powder Technology*, 10(3): 255–27.


## ACKNOWLEDGEMENTS


The authors would like to thank A. Roucoux and A. Nowicki from the 'Synthèe Organique et Systèes Organisé' in Rennes (SOSO), for their collaboration in catalytic tests and synthesis of rhodium colloidal solution. The authors also thank E. Lamouroux, P. Serp from the 'Laboratoire de Catalyse Chimie Fine et Polymèe' in Toulouse, (LCCFP), for nanotubes synthesis experiments with our catalysts.

*The manuscript was received 8 September 2006 and accepted for publication after revision 21 February 2007.*


## APPENDIX A: DETERMINATION OF THE DRYING TIME, $t_{sec}$

In this appendix, a simplified model that permits to evaluate the drying time during the constant drying rate period is presented. This characteristic time can be considered as a reference time.

To determine the drying time, $t_{sec}$, mass and energy balances are carried out at two scales:

- at the reactor scale, global balances make possible to estimate the properties of the fluidized bed atmosphere which surround the particles (bed temperature and average solvent content in gas phase),
- at the particle scale, these balances lead to evaluate the particle temperature and the rate of solvent evaporation flow.

### Balances at Reactor Scale

To establish the balance equations, many simplifying hypothesis are formulated:

- the reactor is considered as a perfect mixer, thus the solvent content in the gas phase is the same in the reactor atmosphere and in the outlet gas flow. This hypothesis is assumed in the case of low bed height and high fluidization gas velocity,
- the bed temperature is supposed to be uniform,
- thermal loss is negligible, the reactor is considered as adiabatic,
- the impregnation step operates in steady state regime,
- the sprayed solution is considered as pure solvent,
- the pulverization gas contents no solvent; it is introduced into the bed at the same temperature as that of the pulverization solution.

Moreover, because of the weak dependence of the specific heat of the solvent (liquid and vapour), and of fluidization gas with respect to the temperature, these magnitudes are considered as constant and their values are determined at the average temperature of the streams.

Solvent mass balance, in the reactor, is given by

$$\dot{m}_{sl} + \dot{m}_{g}^{sec} Y^{e} = (\dot{m}_{g}^{sec} + \dot{m}_{ato}^{sec}) Y^{s} \tag{A1}$$

where, $\dot{m}_{g}^{sec}$, $\dot{m}_{ato}^{sec}$ represent respectively the pulverization and the fluidization dry gas mass flow rate. $\dot{m}_{sl}$ corresponds to the solvent mass flow rate introduced by the system of pulverization and is linked to the sprayed solution flow rate, by the following relation:

$$\dot{m}_{sl} = \dot{m}_{so}\,(1 - c_{l}) \tag{A2}$$

where, $c_{l}$, is the concentration of the precursor in solution expressed in kg of precursor per kg of solution.

$Y^{e}$ and $Y^{s}$, are respectively the solvent gas content at the inlet and at the outlet of the reactor expressed in kg of solvent per kg of dry gas. $Y$ is directly related to the partial pressure of solvent by

$$Y = \frac{M_{sl} p_{sl}}{M_{g}(P_{t} - p_{sl})} \tag{A3}$$

For a fixed bed temperature, the maximum solvent content, noted $Y^{\circ}$, in the reactor can be calculated by the relation A4:

$$Y^{\circ} = \frac{M_{s} P_{sl}^{0V}(T_{bed})}{M_{g}[P_{t} - P_{sl}^{0V}(T_{bed})]} \tag{A4}$$

where, $M_{g}$ and $M_{sl}$, are the molecular weight of fluidization gas and solvent, $P_{sl}^{0V}$, the solvent saturation vapour pressure dependent on the bed temperature, and $P_{t}$ the total reactor pressure. The ratio $Y/Y^{\circ}$ represents the saturation ratio given by A5:

$$\tau_{sat} = \frac{Y}{Y^{\circ}} \tag{A5}$$

In order to achieve the enthalpy balances on the reactor, the following reference states are chosen:

- for fluidization and pulverization dry gases: reference states: gas, $T_{ref} = 273$ K, $P_{ref} = P_{atm}$,
- for the solvent, reference states: liquid, $T_{ref} = 273$ K, $P_{ref} = P_{atm}$,

- for the precursor, reference states: solid, $T_{ref} = 273$ K, $P_{ref} = P_{atm}$.

The global enthalpy balances on the reactor is expressed through equation (A6):

$$\dot{m}_g^{sec}(He_g^e - He_g^s) + \dot{m}_{ato}^{sec}(He_{ato}^e - He_{ato}^s) + \dot{m}_{sl}He_{sl} = 0 \quad \text{(A6)}$$

It should be specified that $He_g$ represents the enthalpy of one kilogramme dry gas to which is associated $Y$ kilogram of solvent vapour. The enthalpies of the inlet and outlet flows are given by

$$He_g^e = C_p^{g,e}T_g^e + Y^e(\Delta H_v^0 + C_{p,sl}^{vap}T_g^e) \quad \text{(A7)}$$

$$He_g^s = C_p^{g,s}T_g^s + Y^s(\Delta H_v^0 + C_{p,sl}^{vap}T_g^s) \quad \text{(A8)}$$

$$He_{ato}^e = C_{p,ato}^g T_{so}^e \quad \text{(A9)}$$

$$He_{ato}^s = He_g^s \quad \text{(A10)}$$

$$He_{sl} = C_{p,sl}^l T_{so}^e \quad \text{(A11)}$$

We note that, $\Delta H_v^0$, is the latent heat of solvent vaporization at the reference temperature, $C_{p,sl}^{vap}$, its specific heat in a vapour state, $C_{p,sl}^l$, its specific heat in a liquid state, $T_{so}^e$ its inlet temperature.

The resolution of the global balances on the reactor make it possible to estimate the inlet gas temperature for a given bed temperature, fluidization gas flow rate and liquid masse flow rate. Moreover, the constraint which imposes the minimal temperature of impregnation is the saturation ratio. It is defined as the ratio between the solvent gas content in the reactor and those at the saturation. For a fixed liquid flow rate, the minimal temperature of the bed corresponds to a saturation ratio close to 1.

This saturation ratio is linked to the relative solvent gas content, RH, by the following expression:

$$\tau_{sat} = RH\frac{P_t - P_{sl}^{0V}(T_{bed})}{P_t - RH \times P_{sl}^{0V}(T_{bed})} \text{ with}$$

$$RH = \frac{p_{sl}}{P_{sl}^{0V}(T_{bed})} \quad \text{(A12)}$$

## Balances at Particle Scale

Generally, the drying rate strongly depends on the nature of solvent present in the wet particle. We can distinguish three periods of drying represented in Figure A.1. The first one is the initial adjustment period (phase 1), during which the energy supplied to the wet particle is used for its heating without modifying in a significant way the solid solvent content.

Generally, this period is short compared to the two other ones following periods:

- The 'constant drying rate period' (phase 2) corresponds to the evaporation of unbound moisture. This second phase of drying, independent of the nature of the solid substrate, is governed by the heat and mass transfer between the gas atmosphere and the surface of the product. Moreover, the temperature of the wet particle in this period remains constant and equal to the wet-bulb temperature.

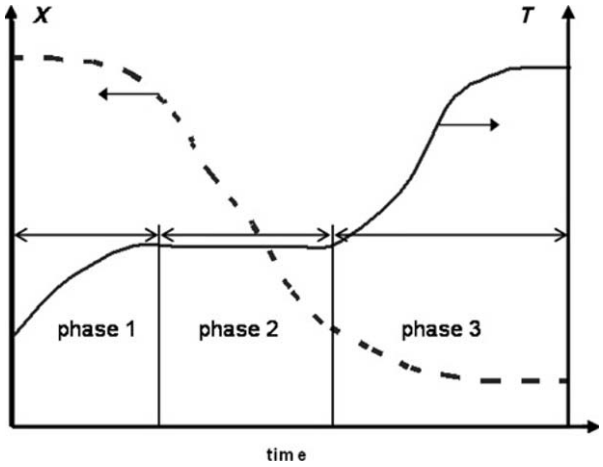


*Figure 13.* Schematization of a drying curve.

- The 'falling-rate period' (phase 3) corresponds to the removal of bound moisture. It is the solvent which is linked at the solid matrix by the interfacial forces, capillary forces, Van der Waals or of hydrogen bonds on the polar group. The mechanism of transfer of solvent inside the solid is complex: we can distinguish the diffusion of the vapour in the solid matrix, the surface migration and the capillarity. During this period, the temperature of the wet particle increases gradually to reach a value close to the temperature of the gas atmosphere.

The evaporation rate during this last period depends on the structure of the product and on the nature of the solution of impregnation. Indeed, Kelvin's law shows that the influence of the interfacial forces on the evaporation of solvent becomes dominating for the mesoporous and microporous solids (average size of the pores lower than 50 nm). Moreover, the presence of organic or inorganic salts dissolved in solvent can modify the thermodynamic properties of solvent, specially its vapour tension.

In our case, in order to estimate the drying characteristic time of a solid particle soaked in solvent, we considered that the drying is carried out in the constant drying rate period. By taking into account the explanations formulated before concerning the difficulty of evaporating bound moisture, this hypothesis leads to a large underestimation of the drying time.

The mass balance on the soaked particle is expressed by (A13):

$$-m_p^{sec}\frac{\partial X}{\partial t} = k_y S_p(Y_i - \bar{Y}) \quad \text{(A13)}$$

in this expression $Y_i$, is the absolute content solvent at the interface, depending essentially on the particle temperature and is expressed according to equation A14.

$$Y_i = \frac{M_{sl}P_{sl}^{0V}(T_p)}{M_g[P_t - P_{sl}^{0V}(T_p)]} \quad \text{(A14)}$$

$k_y$ represent the mass transfer coefficient expressed in kg s$^{-1}$ m$^{-2}$, $S_p$, the external surface of a particle in m$^2$, $m_p^{sec}$, the mass of the dry particle, $X$, the solid solvent content (kg solvent kg$^{-1}$ of dry particle), $\bar{Y}$, the average gas solvent

content in the bed, is taken equal to that in the outlet gas flow ($\bar{Y} = Y^s$).

Concerning, thermal balance on the particle, we considered that the heat flow provided by the fluidized medium is essentially used to compensate the evaporation of the solvent (hypothesis usually employed to describe the constant rate drying period) according to equation (A15):

$$\phi_{th} = hS_p(T_{bed} - T_p) \tag{A15}$$

$$h \times S_p \times (T_{bed} - T_p) = -m_p^{sec}\frac{\partial X}{\partial t} \times (\Delta H_v^0 + C_{p,sl}^{vap} T_{bed} - C_{p,sl}^{l} T_p) \tag{A16}$$

where, $h$ represents the convective heat transfer coefficient expressed in W m$^{-2}$ K$^{-1}$ $C_{p,sl}^{p}$ the specific heat of the wet particle expressed in J kg$^{-1}$ of dry solid K$^{-1}$.

Combining, this equation (A16) with the equation (A13), we obtain the equation (A17):

$$\frac{T_{bed} - T_p}{\bar{Y} - Y_i} = -\frac{k_y}{h}\left(\Delta H_v^0 + C_{p,sl}^{vap} T_{bed} - C_{p,sl}^{l} T_p\right) \tag{A17}$$

In turbulent flow, mass and heat transfer coefficients are linked via the Chilton–Colburn analogy's in the following way:

$$\frac{h}{k_y} = \left(\frac{Sc}{Pr}\right)^{2/3} C_{p,h}^{g} = (Le)^{2/3} C_{p,h}^{g} \tag{A18}$$

where, $Sc$, $Pr$ and $Le$ represent respectively the number of Schmidt, Prandtl and Lewis and $C_{p,h}^{g}$, humid heat of wet gas expressed by

$$C_{p,h}^{g} = C_p^{g} + YC_{p,sl}^{vap} \tag{A19}$$

It should be noted that for an air–water vapour mixture the Lewis number is close to 1. By combining equations (A17) and (A18), we obtain

$$\frac{Y_i - \bar{Y}}{T_p - T_{bed}} = -\frac{C_{p,h}^{g}}{\Delta H_v}(Le)^{2/3} \tag{A20}$$

where $\Delta H_v$ represents evaporation enthalpy of solvent given by

$$\Delta H_v = \Delta H_v^0 + C_{p,sl}^{vap} T_{bed} - C_{p,sl}^{l} T_p \tag{A21}$$

Equation (A20) allows to link the conditions of the interface ($Y_i$ and $T_p$) to the properties of the reactor atmosphere ($T_{bed}$ and $\bar{Y}$ ). In addition, $Y_i$ the solvent content at the interface is directly related to the particle temperature by the means of the saturation vapour pressure of solvent's law. Thus, knowing the solvent content and the temperature of the gas atmosphere surrounding the particle, resolution of the equations (A14), (A20) and the saturation vapour pressure law lead to an estimation of $T_p$ and $Y_i$.

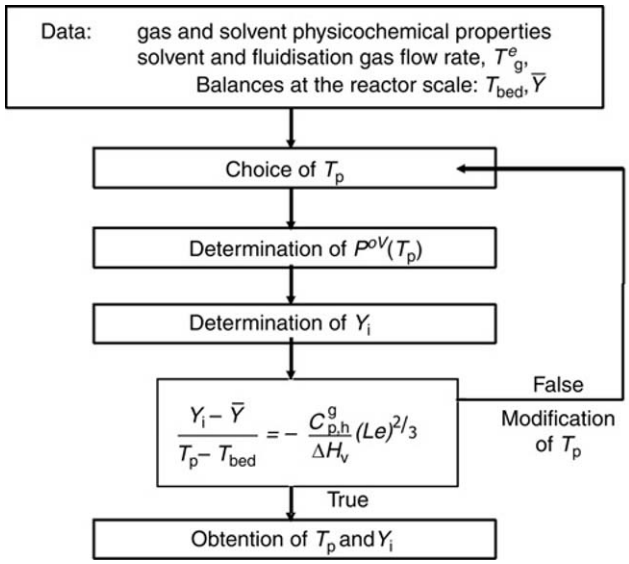


*Figure 14.* Resolution schematization.

The algorithm of resolution of these equations uses an iterative method which is given in the Figure A.2.

The determination of the rate of evaporation requires an estimation of mass and heat transfer coefficients. It has been done using the correlations (Cobbinah, 1984). We obtain a value of 0.11 kg m$^{-2}$ s$^{-1}$ for the mass transfer coefficient. So, the drying characteristic time can be calculated by the equation (A22):

$$t_{sec} = \frac{V_p \chi \rho_{sl}}{S_p k_y(\bar{Y} - Y_i)} \tag{A22}$$

where, $S_p$ and $V_p$ are respectively the particle surface and volume, $\chi$ internal porosity of the particle, $\rho_{sl}$ density of the solvent.

In the case of spherical particles, this equation (A22) becomes

$$t_{sec} = \frac{d_p \chi \rho_{sl}}{6k_y(\bar{Y} - Y_i)} \tag{A23}$$

where, $d_p$ represents the particle diameter.